WPPFC-CPR(17) 16923

J Romazanov et al.

First ERO2.0 modelling of Be erosion and non-local transport at JET ILW

Preprint of Paper to be submitted for publication in Proceeding of 16th International Conference on Plasma-Facing Materials and Components for Fusion Applications

This work has been carried out within the framework of the EUROfusion Consortium and has received funding from the Euratom research and training programme 2014-2018 under grant agreement No 633053. The views and opinions expressed herein do not necessarily reflect those of the European Commission.

First ERO2.0 modelling of Be erosion and non-local transport in JET ITER-like Wall

J. Romazanov[†], D. Borodin[†], A. Kirschner[†], S. Brezinsek[†], S. Silburn[‡], A. Huber[†], V. Huber[†], H. Bufferand[§], M. Firdaouss[§], D. Brömmel[¶], B. Steinbusch[¶], P. Gibbon[¶], A. Lasa[#], I. Borodkina[†], A. Eksaeva[†], Ch. Linsmeier[†], JET Contributors[‖]

[†]Forschungszentrum Jülich GmbH, Institut für Energie- und Klimaforschung – Plasmaphysik, Partner of the Trilateral Euregio Cluster (TEC), 52425 Jülich, Germany
[‡]Culham Centre for Fusion Energy, Abingdon OX14 3DB, UK
[§]CEA, IRFM, F 13108 St Paul-Lez-Durance, France
[¶]Forschungszentrum Jülich GmbH, Institute for Advanced Simulation, Jülich Supercomputing Centre, 52425 Jülich, Germany
[#]Oak Ridge National Laboratory, Oak Ridge, TN 37831-6169, USA

E-mail: `j.romazanov@fz-juelich.de`

May 2017

Abstract. ERO is a Monte-Carlo code for modelling plasma-wall interaction (PWI) and 3D impurity transport for applications in fusion research. The code has undergone a significant upgrade (ERO2.0) which allows increasing the simulation volume to cover the entire plasma edge of a fusion device, allowing a more self-consistent treatment of impurity transport and comparison with a larger number of experimental diagnostics. The physics-relevant technical innovations of the new code version are described and discussed. The new capabilities of the code are demonstrated by the modelling of Beryllium (Be) erosion of the main wall JET limiter discharges. Erosion patterns on the limiters and global Be transport including incident particle distributions are presented. A novel synthetic diagnostic, which mimics wide-angle camera images, is presented and used for validating various aspects of the code, including erosion, shadowing, non-local impurity transport, and light emission calculation.

1. Introduction

The erosion of the first wall (FW) of fusion reactors by sputtering is one of the key challenges on the way to ITER. Erosion affects FW lifetime, plasma impurity content, and also tritium retention via co-deposition. The sputter yields depend not only on

[‖] See the author list of "Overview of the JET results in support to ITER" by X. Litaudon et al. to be published in Nuclear Fusion Special issue: overview and summary reports from the 26th Fusion Energy Conference (Kyoto, Japan, 17-22 October 2016)

surface composition and morphology, but also on the incidence energy and angle of the projectiles. Therefore local wall geometry and plasma conditions including sheath physics have to be taken into account. Additionally, for situations in which impurity sputtering is dominant (e.g. self-sputtering), the charge distributions of the impurities entering the sheath need to be accounted for. Hence, estimating erosion in existing fusion experiments and extrapolation to ITER or DEMO is elaborate and requires modelling of both plasma-wall interaction (PWI) and impurity transport.

The MC code ERO [1] calculates edge impurity transport (including SOL and sheath physics) and PWI in 3D, and has been applied to problems in various fusion experiments. Due to following eroded particles in 3D with full resolution of the gyromotion for ions, the code can efficiently describe effects such as prompt deposition of heavy ions like tungsten (W), and also calculate synthetic diagnostic signals such as spectroscopic line emission for experimental verification. However, a major drawback of ERO is that it was originally designed for simulating selected PFC components, such as TEXTOR test limiters [1]. The cuboid-like simulation volume typically has sizes $\ll 1$ m in poloidal, toroidal and radial directions. It is desirable to increase the volume significantly in order to obtain a more complete and self-consistent model of impurity transport and PWI. This would also make it possible to cross-check experimental diagnostics at different locations for code verification.

To enable simulations of larger volumes, the ERO code has undergone a significant upgrade. While the new version 2.0 relies on the same scientific assumptions as before (details on these can be found in [1]), the volume can now be increased to cover the whole plasma edge of a fusion device in 3D. In this contribution, we introduce ERO2.0 and discuss physics-relevant code improvements, such as the wall geometry model and code parallelization. In order to demonstrate the new possibilities opened up by ERO2.0, we present results for modelling of beryllium (Be) erosion in the main chamber of JET's ITER-like wall (ILW) [2] during limiter discharges. The non-local Be transport and resulting impurity density in the plasma, and also the distributions of incidence energy and angle of Be particles on PFCs are discussed. Additionally, a novel synthetic diagnostic, which mimics experimental wide-angle camera images, is presented and applied for validating modelling results.

2. ERO2.0 code

For easier reference the previous code version will be labeled in the following text as 'ERO1.0', whereas 'ERO' will be used for discussing properties that apply to both versions.

ERO1.0 defines a local coordinate system (x, y, z), with x and y being in-plane with an investigated wall part and z pointing radially away from it. The wall geometry is then described by a function $z(x, y)$. The usage of these local coordinates was convenient for the simulation of selected PFC parts, but is inadequate for larger simulation volumes with complexly shaped wall components. In ERO2.0, the wall geometry is therefore

implemented as a polygonal mesh in 3D. Each polygon is treated as a computational surface cell at which PWI processes are calculated and results are stored. Figure 3 shows the polygon mesh used for the ERO2.0 simulations of the JET ITER-like wall in the present contribution. The mesh resolution can be refined to accurately resolve more details where it is required.

For meshes with large polygon numbers, polygon distance queries in which the distance of a test particle position to the nearest polygon is determined can become the code performance bottleneck, as the computing time of a single query scales linearly with the number of polygons. Therefore, an octree search algorithm has been implemented. This way the query time is not only reduced, but also scales logarithmically with the number of polygons.

ERO requires the plasma background as input, with spatially resolved parameters such as the electron density, electron and ion temperature, ion flow velocity, and electromagnetic fields. In ERO1.0, these were mostly given as 1D profiles or 2D maps. In ERO2.0, it is possible to provide a 3D plasma background. Plasma parameters are stored in nodes of a regular grid and tri-linear interpolation is applied between the nodes. To reduce CPU memory usage, it is possible to apply domain subdivision. In this approach, the 3D data is sub-divided into smaller chunks. For computing a particle trajectory, only the data for the sub-domain in which the particle resides is loaded into memory.

The density of test particles is recorded by ERO on a 3D grid, and can be used e.g. to produce synthetic spectroscopy signals. Typically, a cell size of $\sim$1 mm size in each direction is required for sufficient accuracy. This is again a potential problem for CPU memory. To deal with this, ERO2.0 makes use of the fact that the 3D impurity densities are typically sparse, i.e. only a few percent of cells have non-zero densities. Therefore the particle densities are stored and printed as sparse matrices.

In order to keep computing time affordable even for large volumes, an increased computational performance is required to optimize the code execution time T. For most applications, T is determined by the computationally expensive calculation of particle trajectories, $T \approx n \cdot \langle\tau\rangle$. Here, n is the number of particles and $\langle\tau\rangle$ the mean computing time for a single particle until it either leaves the simulation volume or re-deposits at a PFC. When increasing the simulation volume, two main factors lead to an increase in T: 1) n has to be chosen higher to have sufficient statistics for the transport, because more PFC particle sources are considered, and 2) $\langle\tau\rangle$ increases, because the particle can cover larger distances before leaving the simulation volume or being re-deposited. Therefore ERO2.0 has been massively parallelized, which means each CPU core ('process') of a computer cluster is computing a number of particle trajectories concurrently. Because work loads for different test particles can vary, a dynamic load balancing algorithm was implemented. Instead of distributing equal number of particles across the processes, the algorithm dynamically assigns new particles to those processes that finish earlier, so that in the end all processes finish approximately at the same time.

Figure 1 shows results for a test run to study the speedup of ERO2.0 on the

JURECA supercomputer [3]. The number of processes p is increased from $p = 1$ to $p \approx 1500$. The number of test particles $n(p)$ (which is roughly proportional to the 'work load') is increased proportionally, with $n(1) \approx 1300$. Because each process computes roughly the same amount of particles, the code execution time $T(p)$ should remain constant with p for an ideally parallelized code ('weak scaling'). In figure 1, we observe a mild increase in execution time by a factor of $T(1500)/T(1) \approx (3)$, which is due to the increasing fraction of time each process spends communicating with other processes. Yet the result is positive as it shows that parallelization allows simulating several hundred more test particles with nearly the same execution time.

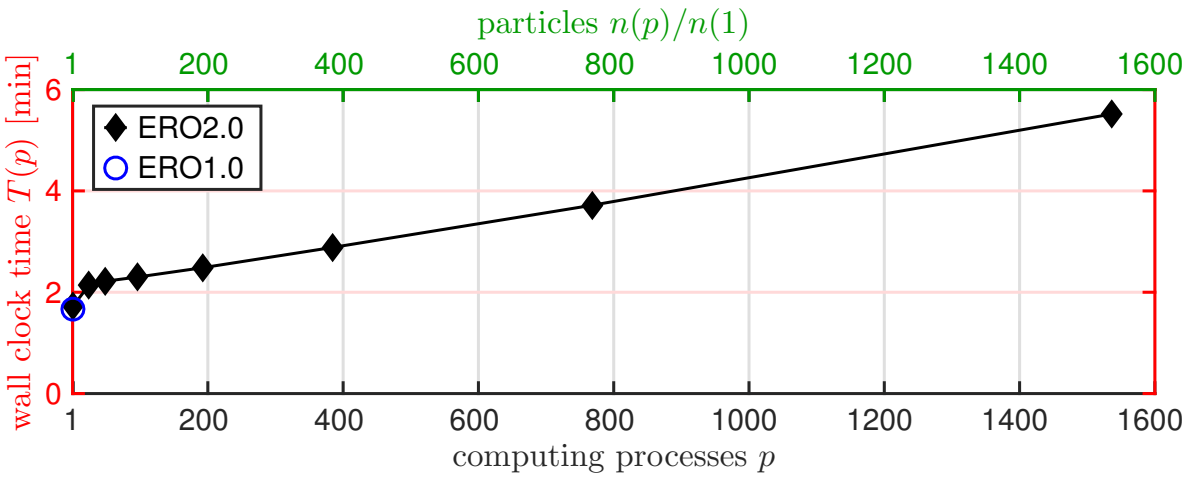

Figure 1: Parallel performance measurements on the Jülich supercomputer JURECA. The number of particles $n(p)$, which is roughly proportional to the problem size, is scaled proportionally to the number of computing processes p ('weak scaling') with $n(1) \approx 1300$. The code execution time $T(p)$ is measured.

3. Experiments and Modelling

The modelling within the present work is based on an experiment dedicated to the determination of Be first wall erosion [4]. In this experiment, a series of limiter plasmas with ohmic heating and contact point at the inner wall (IW) was used to experimentally determine Be yields using line-of-sight (LOS) integrated passive spectroscopy of Be atoms, Be ions and BeD molecules. The last closed flux surface (LCFS) for reference shot JPN #80321 is shown in figure 2a along with the spectroscopy LOS. The gas fuelling rate has been varied ('density scan'), resulting in a variation of electron density and electron temperature which show an inverse relationship. Thus, the dependence of experimental sputter yields on the electron temperature could be determined. These results were recently used for validating the Be sputter yields and Be transport model of ERO1.0 [5].

The present work can be seen as a continuation of [5], but with the simulation volume increased substantially as seen in figure 2a. While the ERO1.0 volume was

limited to the close surroundings of the spectroscopy observation spot, the ERO2.0 volume covers the entire edge of the plasma between the wall and a specified core plasma flux surface ρ_c. The role of the boundary conditions on Be transport results will be discussed below. We focus on the added information provided by ERO2.0, namely the PWI results for a larger set of PFCs, non-local Be transport, and its verification with experimental wide angle camera images.

3.1. Plasma background

The magnetic field $\vec{B}$ for ERO2.0 simulations was taken from EFIT [6]. The required code input parameters of electron density n_e and temperature T_e are based on combined radial profiles from reciprocating probe (RCP), Thompson scattering (TS), embedded probe and spectroscopic measurements. Using the two-point model as described in [7], plasma parameters at a target (wall) location can be calculated from measured values at the upstream location connected by a field line. Using linear interpolation along a field line between target and upstream, *R-Z* maps of the plasma background can be obtained for the full poloidal cross-section. Four maps were used for shots comparable to JPN #80321 in which RCP data were available. These maps were parametrised with the line-integrated density signal from interferometry and interpolated accordingly to obtain plasma backgrounds for specific simulations, e.g. for JET pulse number (JPN) #80321. Figure 2b shows parts of the interpolated electron density and temperature profiles at the inner mid-plane near the LCFS and figure 2c the electron density for the full *R-Z* map.

The maps contain no information about the ion temperature T_i (which was set to the electron temperature), electric field $\vec{E}$ (which was set to zero), or ion flow velocity $\vec{v}_i$. The ion flow velocity, which is directed towards the closest PFC along a field line in the SOL, was previously shown to play an important role in non-local Be transport [7]. Therefore, the 3D ion flow field in the SOL was calculated using the 'simple SOL' model described in [8].

3.2. Wall geometry

The polygon mesh for JET wall components that was used in this work is shown in figure 3 and was provided by the PFCFlux code database [9] and post-processed for ERO2.0 requirements, e.g. unrequired polygons at the backsides of PFCs were removed. The inset in the red box shows the edges of the quadrilateral polygons in order to indicate the typical polygon resolution of ca. 1 cm edge length (the polygon edges should not be confused with the castellation of the tiles, see e.g. [10], which is not resolved by the mesh). The color coding in figure 3 indicates the material composition of the wall elements. The majority tiles from the inner wall guard limiters (IWGL), which are the main erosion zones in limiter plasmas, are made of bulk Be. In the vicinity of neutral beam injection (NBI) shinethrough areas, tiles from IWGL center sections are recessed and clad with Be-coated Inconel or W-coated carbon-fibre composite (CFC) [2]. Due

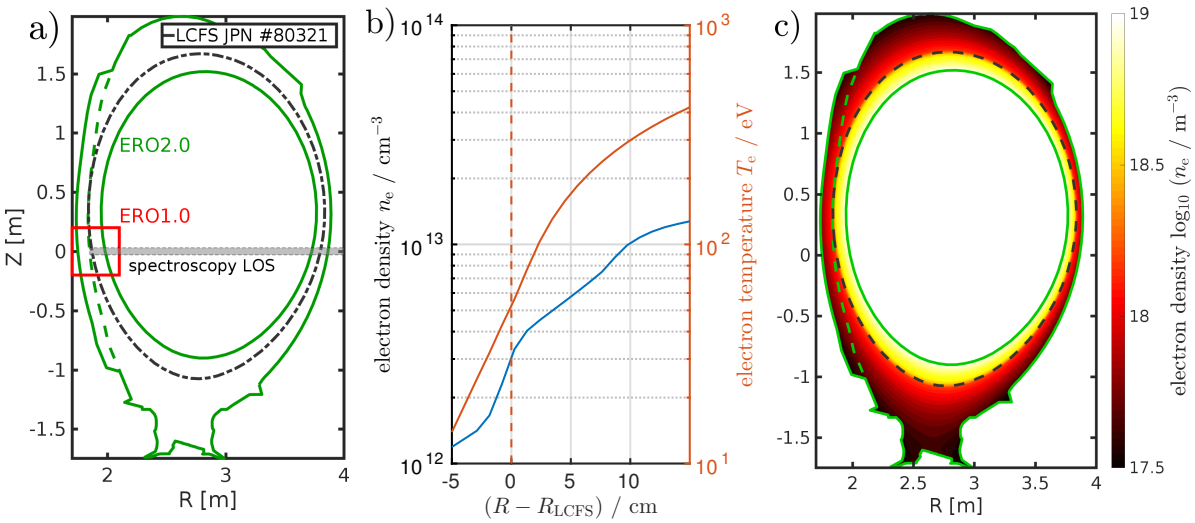

Figure 2: a) Poloidal view of the density scan experiment described in [4][5]. The red solid rectangle shows the boundaries of the ERO1.0 simulation volume. The green contours show the boundaries the new ERO2.0 simulation volume. The dashed lines show the LCFS for JPN #80321 and the ridge of the inner wall guard limiters. b) Profiles of n_e and T_e at the inner midplane near the LCFS, calculated with the two-point model. c) Full R-Z-map of n_e, calculated with two-point model.

to being recessed a few centimeters into the shadowed zone, these tiles shown negligible erosion, therefore only the Be tiles are of interest in this work.

3.3. Sputter yields

For the present modelling Be is assumed to be the only relevant impurity in the deuterium (D) plasma. Consequently only two contributions to Be sputtering are considered, namely physical sputtering by D and by Be (self-sputtering). Chemically assisted physical sputtering (CAPS), which can contribute up to one third of the overall erosion but practically vanishes at high Be limiter temperatures ($T_{surf} > 520°$) [4], was neglected for the present work. ERO uses the Eckstein formula for the sputter yield $Y = Y(E_{in}, \theta_{in})$ [11] in the case of sputtering by test particles for which E_{in} and θ_{in} are known. The Eckstein fit parameters were obtained from molecular dynamics and binary collision approximation calculations, with the assumption of 50 % D content in the Be surface (labeled 'ERO-min' due to yields being 3-4 times lower than for clean Be surfaces), which was recently shown to give good agreement with experiments for plasma-wetted areas [5].

For sputtering by the plasma background, pre-averaged sputter yields $Y = Y(T_e, \alpha)$ are used, with α being the magnetic inclination angle. The pre-averaged yields were obtained from preliminary ERO simulations [5], in which D ions, with Maxwell-distributed energies for a given T_e, are starting at a certain distance from a flat surface, which is inclined by various angles α with respect to the magnetic field.

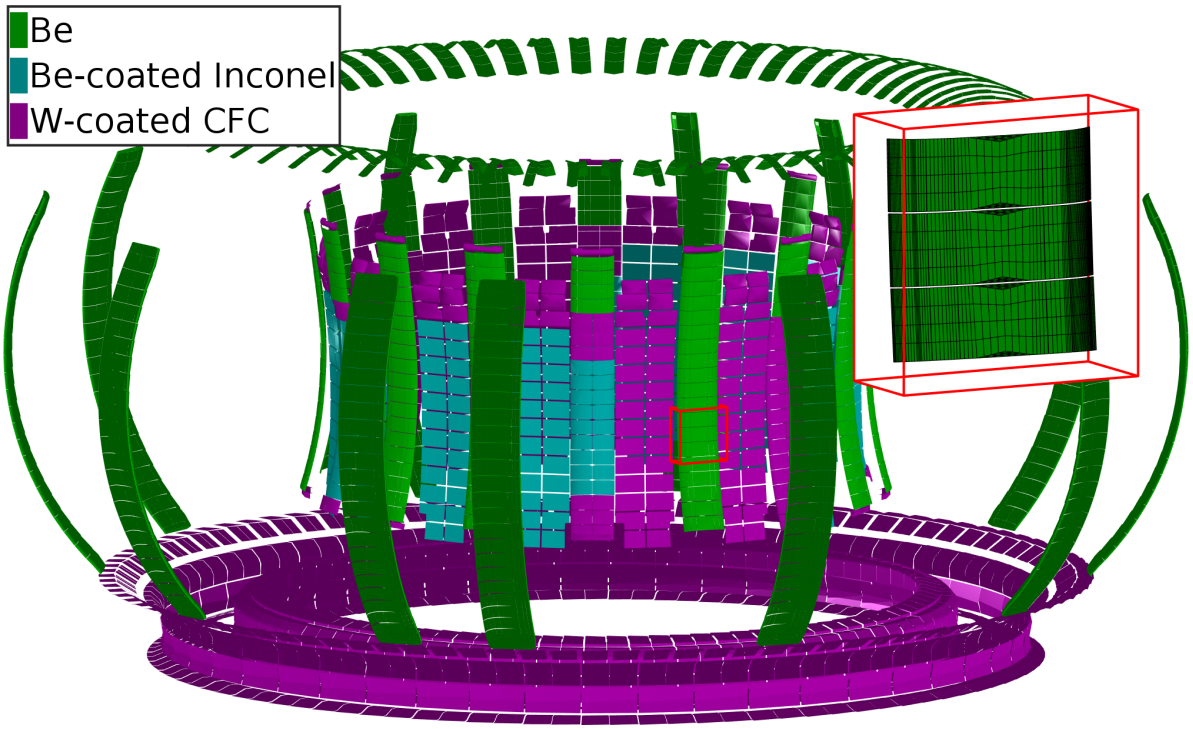

Figure 3: Polygon mesh used by ERO2.0 representing selected wall components of the JET ILW. Polygons are color-coded with material composition. The inset indicates the polygon mesh resolution.

3.4. Modelled erosion of inner wall guard limiter wall tiles

Figure 4 shows exemplarily a selection of surface parameters and PWI results obtained for JPN #80321 at $t = 50$ s. Only the IWGL in JET octant 7X is shown, which is a non-recessed limiter with bulk Be tiles. Figure 4a-b show the electron density n_e and temperature T_e at the sheath entrance respectively, which are the plasma background values evaluated at the surface cell centers. Figure 4c shows the connection lengths L. These were calculated by tracing magnetic field lines from the centers of each surface cell, until either another surface cell is reached or the connection length exceeds the selected threshold $L_{max} = 6\,\mathrm{m}$. The pattern with the inversion at the plasma contact point is characteristic for limiter plasmas and is in good agreement with PFCFlux calculations [9] and heat flux patterns obtained from infra-red (IR) cameras [10].

Figure 4d shows the D ion flux $\Gamma_D^{in} = n_e \cdot c_s \cdot \cos(\alpha) \cdot S$ reaching the surface, with sound speed c_s, magnetic inclination angle θ and 'shadowing factor' S. The latter is introduced as a correction factor between 0 and 1, which accounts for the fact that less ions should reach magnetically shadowed zones. A simple shadowing model with $S = 0$ for cells with $L < L_{max}$ (shadowed) and $S = 1$ for cells with $L = L_{max}$ (plasma-wetted) is used. Figure 4e shows the eroded Be ion flux $\Gamma_{D\to Be}^{ero}$. It is calculated from Γ_D^{in} by multiplying it with the local averaged yields $Y(T_e, \alpha)$.

Figure 4f shows the Be ion flux Γ_{Be}^{in} reaching the surface resulting from the traced

test particles. It should be noted that a non-negligible fraction of particles can reach shadowed zones as well and contribute to $\Gamma^{\mathrm{in}}_{\mathrm{Be}}$. This is not consistent with the shadowing assumption for $\Gamma^{\mathrm{in}}_{\mathrm{D}}$ and identifies the need for a more comprehensive shadowing model in ERO. Such models have already been successfully applied with ERO1.0 in [12] and [13], but were neglected here due to detailed shadowing treatment not being the focus of the very first ERO2.0 application. Figure 4g shows the self-sputtered Be ion flux $\Gamma^{\mathrm{ero}}_{\mathrm{Be}\to\mathrm{Be}}$, which is calculated by multiplying $\Gamma^{\mathrm{in}}_{\mathrm{Be}}$ with the yields $Y(E_{\mathrm{in}}, \theta_{\mathrm{in}})$. Be erosion by self-sputtering $\Gamma^{\mathrm{ero}}_{\mathrm{Be}\to\mathrm{Be}}$ is lower than D sputtering $\Gamma^{\mathrm{ero}}_{\mathrm{D}\to\mathrm{Be}}$, which can be attributed to the incidence Be flux being much lower than the D flux. This can be further quantified by calculating the total number of incidence or eroded atoms per second $n = \sum_i \Gamma_i \cdot a_i$ across all IW surface cells with area a_i. As a rough measure for effective yields, we can define $Y_{\mathrm{eff}} = n^{\mathrm{ero}}/n^{\mathrm{in}}$. Table 1 shows the results. While the effective yield is ∼30 times higher for Be self-sputtering, the Be incidence rate is ∼240 times lower than the D incidence rate, therefore $n^{\mathrm{ero}}_{\mathrm{Be}\to\mathrm{Be}}$ is a factor ∼8 lower than $n^{\mathrm{ero}}_{\mathrm{D}\to\mathrm{Be}}$.

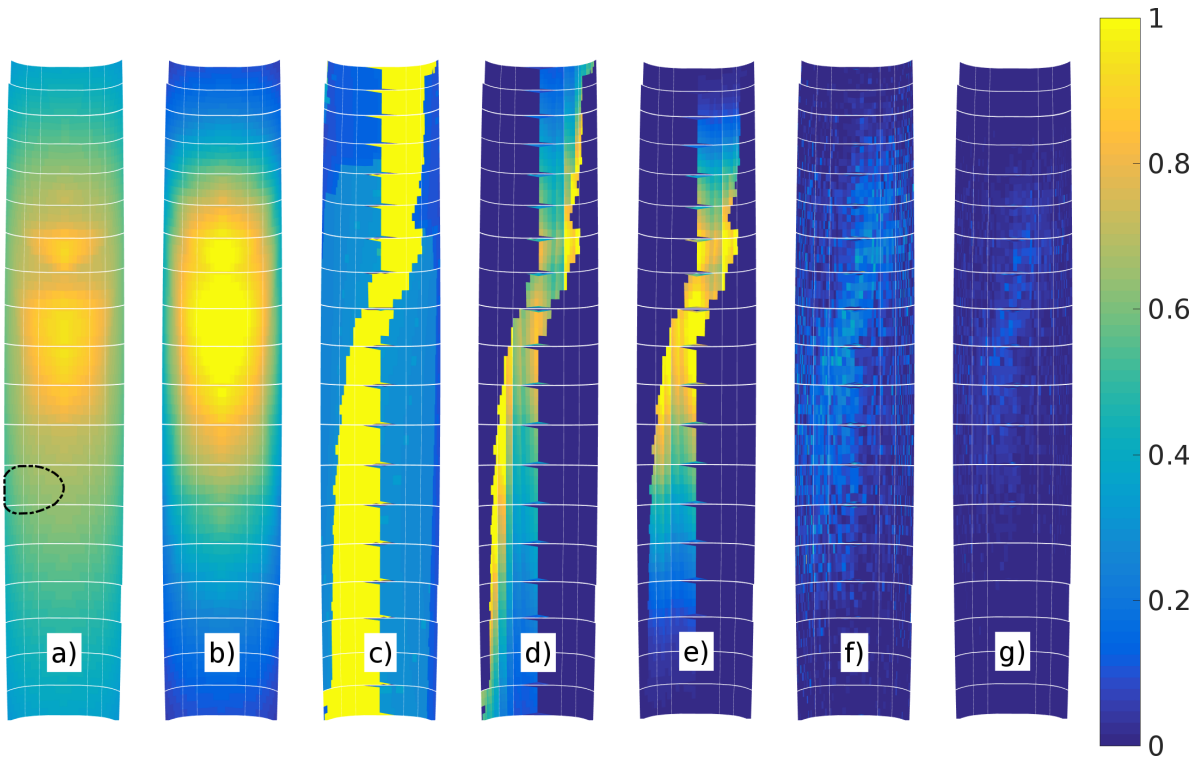

Figure 4: Color-maps (normalized to respective maximum value) of selected surface parameters and PWI results for the IWGL in JET octant 7X. The dashed oval in a) shows the spectroscopic system observation spot used in [4] for determining effective yields. a) Electron density $n_{\mathrm{e}} \,/\, (2 \cdot 10^{12}\mathrm{cm}^{-3})$. b) Electron temperature $T_{\mathrm{e}} \,/\, (30\,\mathrm{eV})$. c) Connection length $L \,/\, (6\,\mathrm{m})$. d) Incidence D flux $\Gamma^{\mathrm{in}}_{\mathrm{D}} \,/\, (10^{18}\mathrm{cm}^{-2}\mathrm{s}^{-1})$. e) D→Be erosion flux $\Gamma^{\mathrm{ero}}_{\mathrm{D}\to\mathrm{Be}} \,/\, (10^{17}\mathrm{cm}^{-2}\mathrm{s}^{-1})$. f) Incidence Be flux $\Gamma^{\mathrm{in}}_{\mathrm{Be}} \,/\, (10^{17}\mathrm{cm}^{-2}\mathrm{s}^{-1})$. g) Self-sputtered Be flux $\Gamma^{\mathrm{ero}}_{\mathrm{Be}\to\mathrm{Be}} \,/\, (10^{17}\mathrm{cm}^{-2}\mathrm{s}^{-1})$.

	D	Be
$n^{\mathrm{in}}\,[s^{-1}]$	$7.6 \cdot 10^{22}$	$3.1 \cdot 10^{20}$
$n^{\mathrm{ero}}\,[s^{-1}]$	$6.2 \cdot 10^{20}$	$8.4 \cdot 10^{19}$
Y_{eff}	0.008	0.27

Table 1: PWI results integrated over all IW tiles. n^{in} are rates of incidence of D and Be particles, n^{ero} are rates sputtering Be particles by D→Be and Be→Be respectively, and Y_{eff} are the corresponding effective yields.

3.5. Modelled Be transport

For understanding the composition of the above $Y_{\mathrm{eff,Be\to Be}}$ value, we need to take into account Be transport results. For the transport calculations, an ensemble of 20^5 test particles was launched. The calculation required $T \approx 2$h on 96 JURECA CPU cores. Figure 5 shows the calculated distribution of incidence Be particles accumulated over all PFC tiles. The angular distribution has its mean at $\theta_{\mathrm{in}} = 50°$ relative to the surface normal. For shallow magnetic field angles relevant for the JET-ILW limiters or ITER blanket modules, similar values are found in literature with ERO1.0 calculations [5] for D ions, and analytic [14] and particle-in-cell calculations [15] for D and carbon (C) ions.

Because charged particles obtain a bulk of their energy from the sheath potential $\Delta E_{\mathrm{in}} = V_{\mathrm{sheath}} \cdot Z \cdot e$, the energy distribution is determined by the distribution of charge state Z, and by the local sheath potential V_{sheath} which is proportional to the electron temperature. ERO2.0 assumes $V_{\mathrm{sheath}} = 3k_{\mathrm{b}}T_{\mathrm{e}}/e$ for the sheath potential. With the maximum $T_{\mathrm{e}} = 30\,\mathrm{eV}$ from figure 4b, the maximum potential is therefore $V_{\mathrm{sheath}} = 90\,\mathrm{V}$. The charge states $Z = 1$, 2 and 3 can well be seen as 'steps' of width 90 eV in the energy distribution. The majority of Be reaches the surface with $Z < 3$.

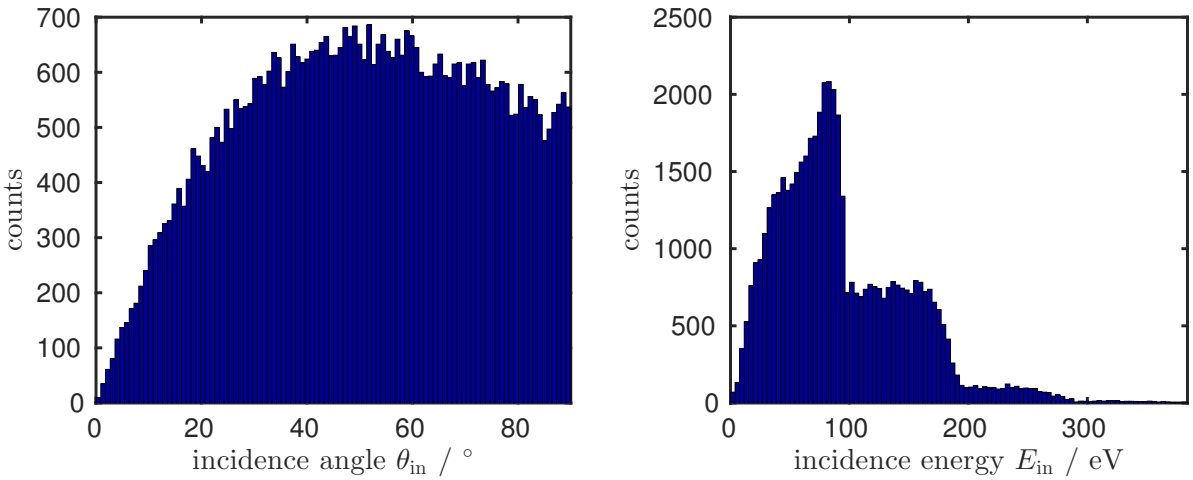

Figure 5: Histograms of Be incidence angle (relative to the surface normal) and energy across all PFC tiles.

Figure 6 shows the simulated Be density for charge states $Z = 1$, 2 and 4 averaged

in toroidal direction and time. For Be^0 (not shown) and Be^+, we observe that the penetration depth (determined by the ionization probability) is in the order of several cm, while recombination from higher ionized Be is negligible. Hence, their density is well localized at the erosion sites on the IW. This leads to the important conclusion that Be I and II line emission measurements in the observation spot must be determined mostly by the Be eroded within the same observation spot or up to a few cm away. This confirms previous determination of LOS-averaged effective yields [4][5], which assumed Be line emission to be originated from particles eroded directly in the observation spot.

From figure 6b-c we see that Be with $Z \geq 2$ penetrates much deeper into the plasma. These particles can in principle reach locations at larger distance from the erosion source after completing one or more poloidal turns and contribute to self-sputtering. However as discussed above, the incidence energy distribution shows only a minor fraction of incident highly ionized Be. This discrepancy can be attributed to the absorbing boundary condition for test particles crossing the ERO2.0 simulation volume boundaries, which are shown as green solid lines in figure 6 and figure 2a. While 55 % of the test particles deposit on the surface of the 3D limiter geometry (and contribute to the histograms in figure 5 and to self-sputtering), the remaining 45 % get absorbed at the boundaries (38 % at the inner and 6 % at the outer boundary).

The outer boundary corresponds to the (R, z) projection of the JET first wall, which was retracted on the left side in order to contain the three-dimensional IWGL surface. The 6 % of particles absorbed at this boundary are travelling into gaps between limiter tiles or onto other PFCs which were not included in the set of 3D polygon meshes (e.g. the Be parallel protection bars below the IWGLs) and are of no further interest in this work. However the 38 % of particles entering the core plasma at the chosen threshold $\rho_c \leq 0.9$ are significant. After being confined in the core plasma for a certain time, particles should re-enter the SOL due to anomalous cross-field transport [8].

This fraction of particles can in principle be accounted for in ERO2.0 by setting ρ_c to smaller values or even dropping it entirely, allowing test particles to freely enter and leave the core plasma. The disadvantage is that calculation time increases dramatically (factor 10 or more) due to the much larger trajectory lengths of the core impurities, which are calculated in full orbit resolution in 3D with small step lengths in ERO. Also, the profile for the anomalous diffusion coefficient $D_\perp$ in the core is not known from first principles (in the edge, it was set to a constant value of $D_\perp = 3$ m^2/s). A potentially better approach currently under investigation is to couple the 3D edge impurity transport calculated by ERO2.0 to a 1D core impurity transport model.

3.6. Synthetic wide-angle camera images

For validating the erosion patterns shown in figure 4 and Be^+ density patterns shown in figure 6, comparison to experimental images from wide-angle cameras can be used. For this purpose, a new synthetic diagnostics which mimics experimental images has been developed in ERO2.0. For rendering images, ERO2.0 can choose between a ray tracing

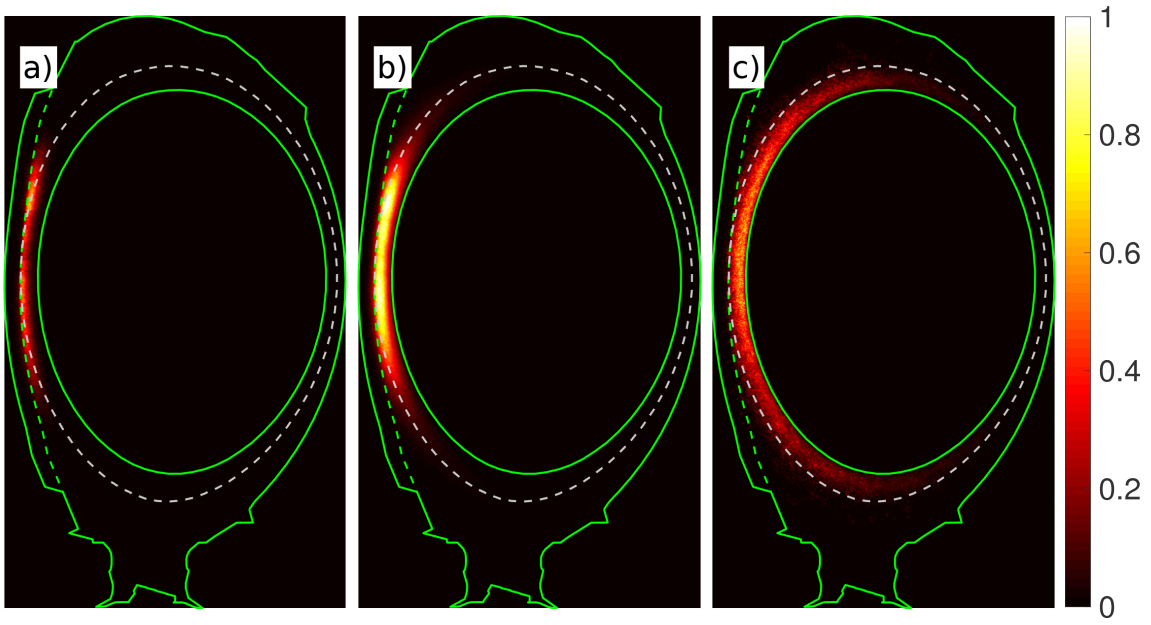

Figure 6: Color-maps (normalized to respective maximum value) showing calculated Be density in R-Z plane averaged over toroidal angle and time. a) $n_{\mathrm{Be}^{+}}$ / $(2 \cdot 10^{16}\mathrm{m}^{-3})$, b) $n_{\mathrm{Be}^{2+}}$ / $(8 \cdot 10^{16}\mathrm{m}^{-3})$, c) $n_{\mathrm{Be}^{4+}}$ / $(2 \cdot 10^{16}\mathrm{m}^{-3})$. Solid white line shows the JET FW, dashed white line shows the separatrix for density scan shot JPN #80321, t=50 s.

algorithm and a perspective projection matrix algorithm. Both algorithms utilize a simple optical model in which the camera is approximated as a pinhole camera with a certain pupil position and LOS direction, however the implementation of the algorithms is different. The ray tracing is more computationally efficient for rendering the wall, while the perspective matrix is more efficient for rendering impurity line emission because ERO2.0 stores 3D emission densities as sparse matrices.

Figure 7a shows the field of view of an experimental camera. The grayscale image was taken from a shot with a disruption flash in which the JET wall is well visible. By fitting selected image points with corresponding points on the CAD 3D wall geometry using the Python module CALCAM, the camera parameters such as the pupil position and LOS could be obtained. Figure 7a shows also a wireframe (red lines) which was rendered by ERO2.0 using these camera parameters. We can see that due to neglecting the optical aberrations of the camera, the image borders deviate from the wireframe more strongly. However, the more relevant image center including several IWGLs shows good match with the wireframe.

As no Be emission images were available from the density scan experiment, instead we use images measured parasitically in limiter discharges (reference shot JPN #91140) with the plasma shifted upward compared to JPN #80321. To obtain a plasma parameters R-Z map as in figure 2c, a translation and 'squeezing' transformation was applied. Figure 7b shows an overlay of the wireframe with the experimental image of Be II 467 nm line intensity (colored) from JPN #91140. Figure 7c shows a similar overlay

for the intensity simulated by ERO2.0. We can see that code can qualitatively well reproduce the emission patterns from the experiment. Because Be^+ is localized at the erosion areas, the image reflects the erosion patterns from Figure 4, with the shadowing pattern as the most striking feature. We observe two distinct emission 'plumes' from the IWGLs in octants 4Z (left side of image) and 5Z (center of image). The emission plume of the IWGL in-between in octant 5X is limited to the five tiles at the top, because the other tiles are recessed and therefore not eroded.

Some subtle differences between experiment and modelling are yet visible, which are marked with regions I-III in the figure. In region I, the emission plumes at the IWGLs in the experimental image extend more in z-direction up to the top IWGL tiles compared to the synthetic image. This might indicate that the T_e in the ERO2.0 plasma background has a too strong decay in the scrape-off layer, so that the upper tiles do not get eroded in the modelling. In region II, the plume in octant 5Z has a different shape: it is thinner near the plasma contact point and becomes broader near the limiter ends in experiment, while in the modelling the plume has approximately equal thickness everywhere which is also seen in the Be^+ density in figure 6a. This again might be due to uncertainties in the plasma background used for modelling. The plume width should be determined by ionization rates for Be^+ and Be^0 and also by photon emissivity coefficients (PEC). Both ionization rates and PECs are obtained from ADAS [16] and are dependent on T_e and n_e. However the dependency is rather weak, e.g. if taking a 2 times higher T_e at the separatrix, the ionization rate increases by 30 % while the PEC decreases by 8 %. A more comprehensive benchmarking would require comparison to Be I experimental images which were not available yet. Finally in region III, an emission plume is visible in the experimental image below the 5Z IWGL which is missing from the synthetic image. This can be attributed to erosion of the Be parallel protection bars, which are currently missing in the ERO2.0 wall geometry.

4. Conclusions

The new code version ERO2.0 has been developed which contains several principal technical innovations, such as a more flexible definition of wall geometry and increased computational efficiency due to parallelization which allows to simulate several hundred more particles within the same computing time as before. These innovations allow significant increase of the simulation volume. To demonstrate the new modelling capabilities resulting from this, simulations for JET limiter plasmas were performed.

The magnetic connection length patterns show good agreement with PFCFlux calculations and IR measurements. Erosion patterns due to D and Be impact were calculated. The erosion rate due to D impact was shown to be 8 times higher than Be self-sputtering. The distributions of incident Be were discussed, with the mean incidence angle being 50° and most Be reaching the surface with $Z < 3$. However, the calculations did not take into account Be particles re-entering the SOL from the core plasma. The modelled self-sputtering is therefore currently underestimated. To address

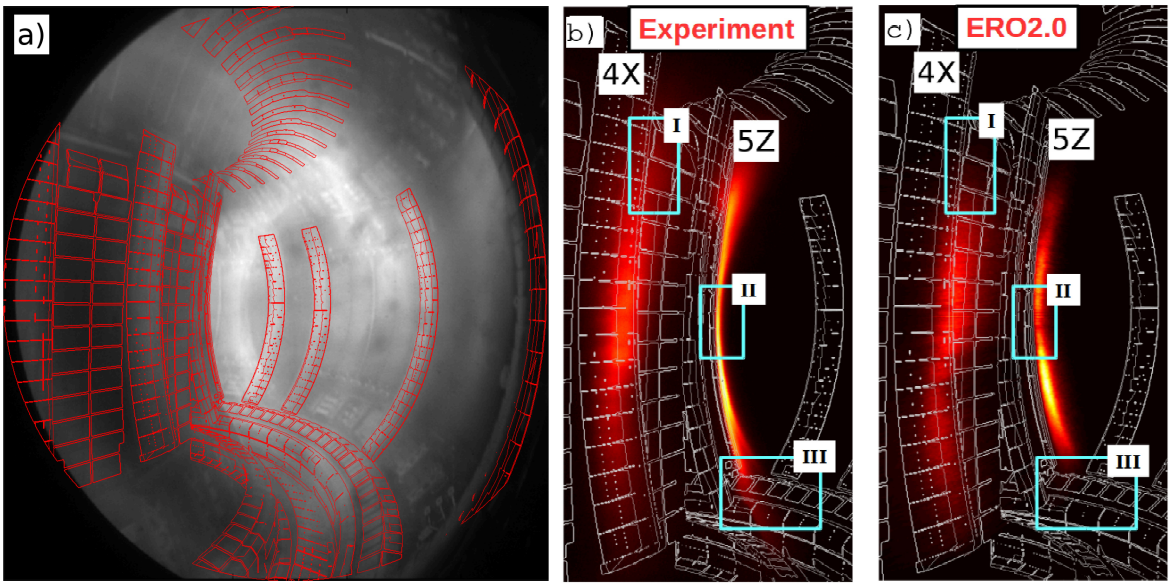

Figure 7: a) Comparison of JET wide-angle camera (KL1-E4WC, Be II 467 nm filter) with synthetic camera of ERO2.0. Grayscale image is a reference image of a disruption shot in which the first wall is fairly visible. Red wireframe was rendered by ERO2.0. b) Overlay of the ERO2.0 wireframe with experimental image from JPN #91140 of the same camera showing Be II emission. c) The same, with Be II emission rendered from ERO2.0 simulation.

this, coupling edge impurity transport in ERO2.0 to a core impurity transport model is under investigation.

A novel synthetic diagnostic has been developed, which uses calculated 3D impurity density to render synthetic wide-angle camera images. These show good qualitative agreement with the respective experimental images for Be II line emission, which increases confidence in the PWI and impurity transport model. Remaining deviations from experiment can largely be attributed to uncertainties in the plasma background, which was currently calculating using the two-point model. To improve this, dedicated modelling of JET limiter plasma backgrounds using the edge code SOLEDGE2D [17] are currently ongoing. Alongside with additional experimental benchmarking, such as with Z_{eff} measurements or with wide-view camera images and LOS-integrated signals of Be line emission, this should provide a more comprehensive and self-consistent modelling of Be erosion and allow more accurate predictions for ITER.

Acknowledgements

This work has been carried out within the framework of the EUROfusion Consortium and has received funding from the Euratom research and training programme 2014-2018 under grant agreement No 633053. The views and opinions expressed herein do not necessarily reflect those of the European Commission. Computer time on JURECA

was provided by the Jülich Supercomputing Centre.

References

[1] Kirschner A, Philipps V and Winter J 2000 *Nucl. Fusion* **40** 989 URL http://dx.doi.org/10.1088/0029-5515/40/5/311

[2] Matthews G F, Beurskens M, Brezinsek S, Groth M, Joffrin E, Loving A, Kear M, Mayoral M L, Neu R, Prior P, Riccardo V, Rimini F, Rubel M, Sips G, Villedieu E, de Vries P, Watkins M L and EFDA-JET Contributors 2011 *Phys. Scr.* **T145** 014001 ISSN 0031-8949 URL http://stacks.iop.org/1402-4896/2011/i=T145/a=014001?key=crossref.0af5621e75d3c560c1ba3bda6a0ccf02

[3] Jülich Supercomputing Centre 2016 *Journal of large-scale research facilities* **2** URL http://dx.doi.org/10.17815/jlsrf-2-121

[4] Brezinsek S, Stamp M, Nishijima D, Borodin D, Devaux S, Krieger K, Marsen S, O'Mullane M, Bjoerkas C, Kirschner A and JET EFDA Contributors 2014 *Nucl. Fusion* **54** 103001 ISSN 0029-5515 URL http://stacks.iop.org/0029-5515/54/i=10/a=103001?key=crossref.1053e645f9929006a4f45aca550d2b55

[5] Borodin D, Brezinsek S, Miettunen J, Stamp M, Kirschner A, Björkas C, Groth M, Marsen S, Silva C, Lisgo S W, Matveev D, Airila M and Philipps V 2014 *Phys. Scr.* **T159** 014057 ISSN 0031-8949 URL http://stacks.iop.org/1402-4896/2014/i=T159/a=014057

[6] Brix M, Hawkes N C, Boboc A, Drozdov V, Sharapov S E and Contributors J E 2008 *Rev. Sci. Instrum.* **79** 10F325 ISSN 0034-6748 URL http://aip.scitation.org/doi/10.1063/1.2964180

[7] Miettunen J, Groth M, Kurki-Suonio T, Bergsåker H, Likonen J, Marsen S, Silva C and Äkäslompolo S 2013 *J. Nucl. Mater.* **438** S612–S615 ISSN 00223115 URL http://dx.doi.org/10.1016/j.jnucmat.2013.01.128

[8] Stangeby P C 2000 *Plasma Phys. Control. Fusion* **43** 223–224 ISSN 0741-3335

[9] Firdaouss M, Riccardo V, Martin V, Arnoux G and Reux C 2013 *J. Nucl. Mater.* **438** S536–S539 ISSN 00223115 URL http://dx.doi.org/10.1016/j.jnucmat.2013.01.111

[10] Arnoux G, Farley T, Silva C, Devaux S, Firdaouss M, Frigione D, Goldston R, Gunn J, Horacek J, Jachmich S, Lomas P, Marsen S, Matthews G, Pitts R A, Stamp M and Stangeby P 2013 *Nucl. Fusion* **53** 073016 ISSN 0029-5515 URL http://stacks.iop.org/0029-5515/53/i=7/a=073016?key=crossref.4107eea369c358b4d22e968611a90c6f

[11] Eckstein W 2008 *Vacuum* **82** 930–934 ISSN 0042207X

[12] Lasa A, Klepper C C, Borodin D, Kirschner A, Groth M, Borodkina I, Safi E and Nordlund K 2015 ERO modelling of RF-Induced Erosion at Antenna-Connected Beryllium Limiters in JET *APS Meeting Abstracts*

[13] Ding R, Pitts R, Borodin D, Carpentier S, Ding F, Gong X, Guo H, Kirschner a, Kocan M, Li J, Luo G N, Mao H, Qian J, Stangeby P, Wampler W, Wang H and Wang W 2015 *Nucl. Fusion* **55** 023013 ISSN 0029-5515 URL http://stacks.iop.org/0029-5515/55/i=2/a=023013?key=crossref.d7accbec2b6a92abbed04c7bbcc3729f

[14] Schmid K, Mayer M, Adelhelm C, Balden M, Lindig S and Team t A U 2010 *Nucl. Fusion* **50** 105004 ISSN 0029-5515 URL http://stacks.iop.org/0029-5515/50/i=10/a=105004?key=crossref.d065bc9371e932610b1ad88d16845c0b

[15] Kawamura G, Tomita Y and Kirschner A 2013 *J. Nucl. Mater.* **438** S909–S912 ISSN 00223115 URL http://www.sciencedirect.com/science/article/pii/S0022311513002055

[16] Summers H P and O'Mullane M G 2005 *The Atomic Data and Analysis Structure* (Berlin, Heidelberg: Springer Berlin Heidelberg) pp 399–413 ISBN 978-3-540-27362-2 URL http://dx.doi.org/10.1007/3-540-27362-X{_}18

[17] Bufferand H, Bensiali B, Bucalossi J, Ciraolo G, Genesio P, Ghendrih P, Marandet Y, Paredes A,

Schwander F, Serre E and Tamain P 2013 *J. Nucl. Mater.* **438** S445–S448 ISSN 00223115 URL http://dx.doi.org/10.1016/j.jnucmat.2013.01.090